

Surface Bubble Growth in Plasmonic Nanoparticle Suspension

Qiushi Zhang, Robert Douglas Neal, Dezhao Huang, Svetlana Neretina, Eungkyu Lee,*
and Tengfei Luo*Cite This: *ACS Appl. Mater. Interfaces* 2020, 12, 26680–26687

Read Online

ACCESS |

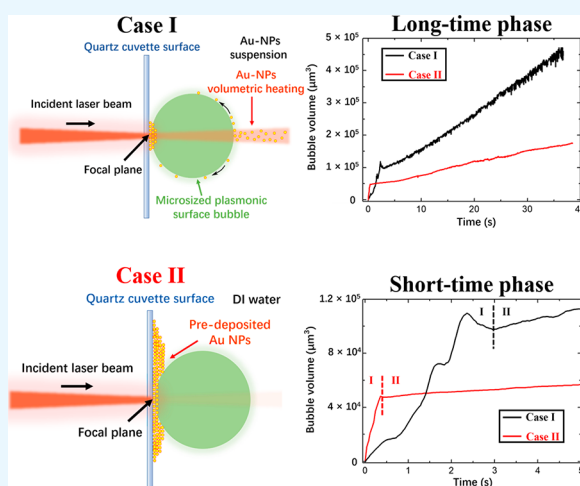
Metrics & More

Article Recommendations

Supporting Information

ABSTRACT: Understanding the growth dynamics of the microbubbles produced by plasmonic heating can benefit a wide range of applications like microfluidics, catalysis, micropatterning, and photothermal energy conversion. Usually, surface plasmonic bubbles are generated on plasmonic structures predeposited on the surface subject to laser heating. In this work, we investigate the growth dynamics of surface microbubbles generated in plasmonic nanoparticle (NP) suspension. We observe much faster bubble growth rates compared to those in pure water with surface plasmonic structures. Our analyses show that the volumetric heating effect around the surface bubble due to the existence of NPs in the suspension is the key to explaining this difference. Such volumetric heating increases the temperature around the surface bubble more efficiently compared to surface heating which enhances the expelling of dissolved gas. We also find that the bubble growth rates can be tuned in a very wide range by changing the concentration of NPs, besides laser power and dissolved gas concentration.

KEYWORDS: gold nanoparticles (NPs), plasmon resonance, photothermal, microbubbles, pulsed laser, volumetric heating, bubble growth dynamics



INTRODUCTION

Plasmonic bubbles can be generated in noble metal plasmonic nanoparticle (NP) suspensions upon the irradiation of a pulsed laser due to the enhanced plasmonic resonance.^{1–6} Incident light at the surface plasmonic resonance can cause the strong oscillation of the free electrons in NPs. Because of electron–phonon coupling, the energy of these hot electrons is quickly transferred to the lattice to intensely raise the temperature of NP, which induces the nucleation of plasmonic bubbles. Microsized bubbles can play important roles in a wide range of applications, including biomedical imaging,^{7–10} healthcare diagnosis,^{11–15} microfluidic bubble logics,¹⁶ pulsed laser ablation in liquid (PLAL),^{17–23} and optothermal micro-bubble-assisted manufacture.^{24–26} In recent years, studies on the growth dynamics of plasmonic surface bubbles have attracted significant attention.^{6,27–33} As discussed before,²⁷ the growth of surface bubbles can be generally divided into two phases, i.e., short-time and long-time growth phases. In the short-time growth phase (phase I), the surface bubble experiences an explosive nucleation due to the vaporization of the liquid surrounding NPs on the surface. In the long-time growth phase (phase II), the bubble growth is mainly because of the expelling of dissolved gas from the liquid surrounding the nucleated surface bubbles.

Plasmonic metal nanoclusters on substrates and submerged in deionized (DI) water have been used previously to study the growth dynamics of plasmonic surface bubbles.^{6,27–33} In this type of experimental systems, surface bubbles usually have an extremely short (10 ms to hundreds of milliseconds) phase I (vaporization-dominated growth), in which the bubbles grow very fast (on average 10^6 – 10^7 $\mu\text{m}^3/\text{s}$), and the volume growth is proportional to \sqrt{t} , where t is time. Compared to phase I, phase II (dissolved air expelling-dominated growth) lasts much longer (e.g., bubbles can be stable for minutes or even more depending on the growth environment), and the volume growth of surface bubble is much slower and linear in time ($\sim 10^4$ $\mu\text{m}^3/\text{s}$). Although the two growth phases are different, the fundamental cause is the same—plasmonic heating of metal nanoclusters on substrates. In addition to ref 27, different behaviors and mechanisms of plasmonic surface bubbles have been investigated and proposed in other studies. For example, Wang et al. have revealed the giant and oscillating

Received: March 25, 2020

Accepted: May 13, 2020

Published: May 13, 2020



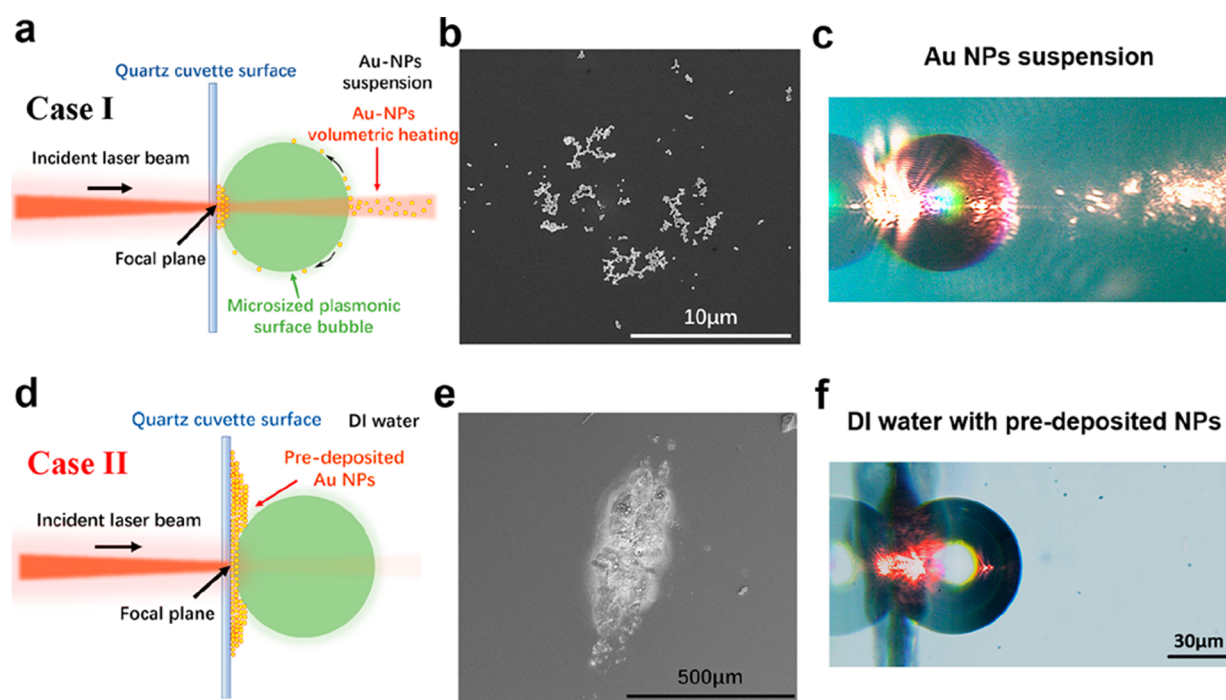


Figure 1. Schematic descriptions of microsized plasmonic surface bubble growth in (a) Au NP suspension (case I) and (d) DI water with predeposited NPs on surface (case II). Scanning electron microscope (SEM) images of predeposited Au NPs at the bubble nucleation site in (b) case I and (e) case II. Optical images from the side view of a plasmonic surface bubble under laser illumination in (c) case I and (f) case II. Scale bar is the same in (c) and (f). The bright regions in (c) and (f) are from the laser scattered by either predeposited or suspended Au NPs.

plasmonic surface bubble in the very early life phase. This is due to the composition of the surface bubble in the early life phase gradually changing from vapor to gas.²⁸ Baffou et al.²⁹ and Zaytsev et al.³⁰ have studied the bubble shrinkage behavior. Because the surface bubble in the long-time growth phase is mainly made of dissolved gas, it displays a linear and slow diffusion-dominated volume shrinkage in air equilibrium water with turning-off the incident laser. Liu et al.⁶ and Chen et al.³¹ have studied the bubble growth dynamics on gold nanoarrays. They found that the volume growth rate of bubble is largely related to the density and geometry of these nanoarrays, which both influence the collective input heating power. Zhao et al.³⁴ and Lin et al.³⁵ have shown the convective flow around surface bubble can be used to trap nano- or microparticles. This originates from the Marangoni flow surrounding the surface bubble. This Marangoni flow is attributed to the temperature gradient formed around the microsize surface bubble.^{32,36–39} In addition to predeposited nanostructures, generating surface bubbles directly by using the plasmonic heating of NP suspension has also been demonstrated.^{40–42} In Richardson et al.'s work,⁴⁰ the theoretical model of light-to-heat conversion efficiency in NP suspension is established from fitting the experimental data of a droplet on the millimeter scale. The adsorption and conversion efficiencies highly depend on the concentration of NPs and input laser power. Armon et al.⁴¹ have demonstrated that bubble movement in NP suspension can be used for micropatterning. Compared to predeposited optically resistive nanostructures, plasmonic NP suspensions feature the advantages of simpler fabrication procedures, higher heating efficiency, and potentially better compatibility with biological environments. Fundamentally, plasmonic NP suspensions are subjected to volumetric heating wherever the excitation laser beam covers, instead of only surface heating as in the

predeposited nanostructure cases. However, detailed investigation of the plasmonic surface bubble growth in NP suspensions has not yet been performed despite their importance for myriad potential applications.

In this paper, we systematically study the growth dynamics of surface bubbles in plasmonic NP suspensions via experiments accompanied by theoretical analyses. Microsized plasmonic surface bubbles are generated with both predeposited NPs clusters and NP suspensions under the irradiation of a pulsed laser at the surface plasmon resonance (SPR) peak of the NP suspension. The growth dynamics of the surface bubbles in both conditions are investigated and compared by using high-speed videography. It is demonstrated that under the same laser conditions (e.g., power density) the surface bubbles grow much faster in the NP suspensions than in DI water with predeposited NPs. Our analysis indicates that it is the volumetric heating in the NP suspension that leads to a higher heating efficiency, which results in higher temperature around the surface bubble and thus larger bubble growth rates. In addition, we also find that the bubble growth rate can be tuned efficiently by changing the concentration of NP in suspension, besides laser power and dissolved gas concentration.

RESULTS AND DISCUSSION

We first study the plasmonic surface bubble growth dynamics in two comparing cases. In case I, we generate microsized surface bubbles on a bare quartz surface immersed in a NP suspension, as shown in Figure 1a. In case II, the bubbles are generated on a quartz surface predeposited with NP clusters immersed in DI water, as shown in Figure 1d. In both cases, pulsed laser excitations are used, and the beams are focused on the quartz/suspension (or/DI water) interfaces (see the [Experimental Methods](#) section for details). In case I, a surface

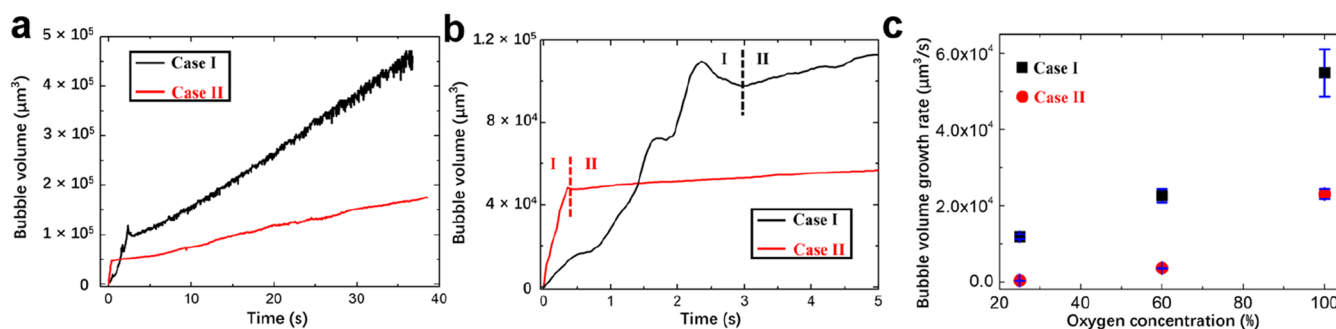


Figure 2. (a) Surface bubble volume as a function of time in the two cases. Both are from liquids with 60% degassing level and the same laser power of ~ 1.1 W. (b) Plot showing a zoomed-in view of the range from 0 to 5 s in (a). (c) Averaged surface bubble volume growth rates of phase II in the two cases under different degassing levels (error bars are included).

bubble nucleates in a few seconds upon laser irradiation. During the short period before bubble nucleation, a small number of NPs are found deposited on the quartz surface as shown in the SEM image in Figure 1b (also see the Supporting Information, Figure S1, which has the SEM images with the $500 \mu\text{m}$ scale bar). The van der Waals interaction between the NPs and surface makes this deposition relatively robust.⁴³ The NPs are deposited due to the negative optical scattering forces as recently revealed in ref 44. Generally, the femtosecond pulsed laser we used in our experiments allows us to generate nanobubbles formed around individual suspended NPs with much lower optical fluence.^{12,13} A femtosecond pulse in the laser train can deliver an amount of energy within ~ 100 fs (generally, the pulse duration is smaller than the electron–phonon coupling time constant), so that the NPs can efficiently deposit the energy to increase the temperature while minimizing the dissipation of heat to the surrounding water. However, when the duration of pulse increases to nanoseconds, microseconds, or infinite (i.e., CW laser), the deposited energy on the NPs during a pulse can be dissipated into the surrounding medium while the duration of a pulse remains. As discussed in ref 44, the nanobubble/water interface at the side of light propagation can redirect the photon flux into backward like a macroscopic optical mirror. When the NP is located in the nanobubble at the side of the light incident, the backward photon stream strikes the surface of NP and thus induces an optical scattering pulling force against the laser incident. Because of this optical pulling force, these NPs are finally deposited and work as optothermal heating sources and nucleation centers for the surface bubble generation. We notice that the area with deposited NPs on the quartz surface is about $\sim 100 \mu\text{m}^2$, comparable to the laser beam cross-sectional area. When the $10\times$ objective lens is used, the $1/e^2$ length of our Gaussian laser spot is $\sim 22 \mu\text{m}$ as determined from a beam profiler. This means that once the surface bubble nucleates and grows, these deposited NPs will be mostly in contact with the gaseous phase, which limits their effectiveness of heating the liquid in the phase II growth due to the large thermal resistance of the gaseous phase.^{45–47} The volumetric heating in the irradiated area due to absorption of the suspended NPs acts as a second heating source in conjunction with the deposited NPs acting as a surface heater, as described in Figure 1a. These NPs can provide additional heat to the liquid around the surface bubble during the entirety of the growth period.

On the other hand, the condition where a surface bubble grows in case II (DI water with predeposited NPs on surface)

has two major differences compared with case I, as illustrated in Figure 1d. First, case II has a much larger amount of NPs predeposited on the surface, which can lead to stronger surface heating. As shown in Figure 1e (also in Figure S1), it is easy to see there are many more Au NPs predeposited on the surface in case II than in case I. Second, since the surface bubble is surrounded by DI water rather than NP suspension in case II, there is no volumetric heating, leaving surface heating as the only heating source. This can be visually observed from the glowing spots in the optical images of surface bubbles under laser illumination, as shown in Figure 1c,f. These glowing spots correspond to the scattered light from the plasmonic Au NPs, either deposited on the surface or suspended in liquid. As seen from Figure 1c,f, there are glowing spots both on the surface and in the laser beam covered volume on top of the bubble in case I, while there are only such glowing spots on the surface in case II.

Because the two cases have distinct heating geometries, different bubble growth behaviors are expected. We record and compare the bubble growth dynamics in the two cases using high-speed videography when they are subject to the same laser irradiation conditions. Recall that surface bubble growth experiences two phases, i.e., the explosive vaporization (phase I) and gas expelling (phase II). As shown in Figure 2a, the bubble in case II undergoes a very fast growth in phase I, with the duration of shorter than 500 ms. The reason for this fast growth is that the large amount of heat from the highly dense NPs predeposited at the surface in case II can quickly lead to a high surface temperature to vaporize water. After the bubble contact line circle is larger than the laser spot size as the bubble grows larger, the heated predeposited NPs can no longer maintain the liquid–vapor interface of the bubble above the vaporization temperature due to the large vapor thermal resistance. This causes the bubble growth to slow down and transition into phase II, which is displayed as a kink in the volume growth plot (Figure 2a,b). On the other hand, in the NP suspension (case I), the phase I bubble grows much slower than that in case II, which can be attributed to the much fewer NPs on the surface as heating sources (see Figure 1b,e). However, it is interesting to see that in the NP suspension the bubble has longer phase I growth (~ 3 s) and reaches a larger size at the end of this period. This is likely due to that the volumetric effect in NP suspension can provide higher heating efficiency than surface heating, which is shown in later discussions. The higher heating efficiency can maintain the evaporation of the water surrounding surface bubble at a larger bubble size. During this longer phase I, the oscillations of the

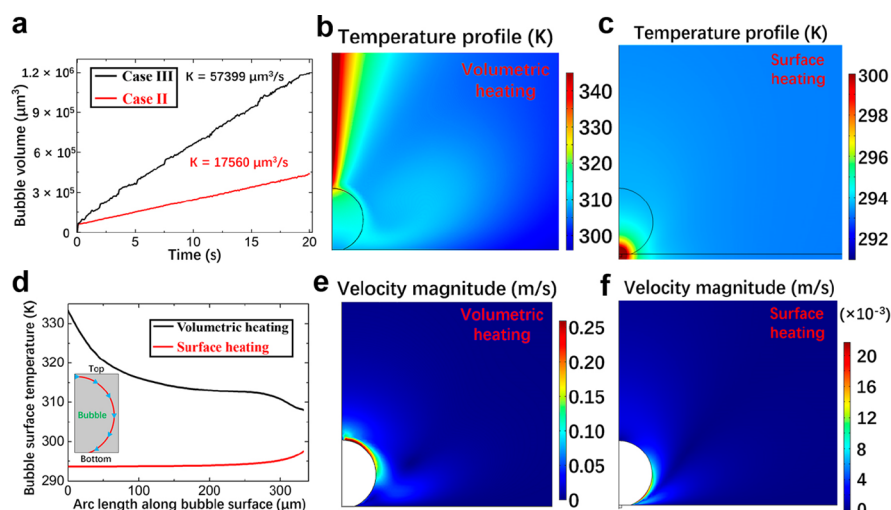


Figure 3. (a) Surface bubble volume as a function of time in DI water (case II) and NP suspension (case III), both with the same amount of predeposited Au NPs and the same laser power of ~ 1.1 W. The volume growth rates (κ) in phase II are shown in the plots. The simulated temperature profiles in the (b) volumetric heating and (c) surface heating cases. (d) Simulated bubble surface temperature from the top to the bottom of the bubble in the two cases. The simulated liquid flow velocity magnitude contours in the (e) volumetric heating and (f) surface heating cases.

bubble volume are also observed, which is similar to the behaviors in ref 28.

Phase II growth usually lasts much longer than phase I. As shown in Figure 2a, both cases have linear volume growth in phase II, consistent with the growth behavior of phase II gas bubbles in previous works.²⁷ In our cases, the plasmonic surface bubble growth is resulted by the local gas oversaturation produced by the enhanced plasmonic heating effect of Au NPs. Unlike the diffusive bubble growth observed in the studies of microelectrode heating,⁴⁸ the bubble volume growth induced by local gas oversaturation is linear in phase II.²⁷ However, there is a clear difference between the growth rates in the two cases, with the NP suspension showing a much higher growth rate. Because phase II growth is due to dissolved gas expelling at elevated temperatures, we then have performed the same experiments but with different degassing levels (see the Experimental Methods section for details). As shown in Figure 2c, the phase II bubbles always grow faster in the NP suspension (case I) than in DI water with predeposited NPs (case II) disregarding the degassing levels. When the dissolved gas is reduced to a very low level (e.g., $\sim 25\%$), the surface bubble in case I still maintains a significant growth rate, while that in case II hardly grows.

To reveal the mechanism of the different phase II growth behaviors, we have first confirmed that the compositions of the bubble in both cases are dissolved gas rather than vapor. As the bubble shrinkage study in the Supporting Information (SI2) evidenced, the shrinkage of our plasmonic surface bubble in phase II is very slow, taking more than 30 min. If it is a vapor bubble, it would collapse immediately (in milliseconds) when the thermal excitation is turned off.⁴⁹ Moreover, our bubble shrinkage is linear with a very slow bubble shrinkage rate ($\sim 420 \mu\text{m}^3/\text{s}$, see Figure S3). As discussed in ref 30, the linear bubble volume shrinkage in gas-saturated water is due to the fact that we can take the limiting case with no gas concentration gradient in the system. In addition, this shrinkage rate is of the same order of magnitude as reported in ref 29, and it is proved that the bubble shrinkage in our cases has a feature of expelled gas redissolving into liquid as the

temperature around the bubble slowly decreases. With this confirmed, we examined the difference in heating sources (i.e., surface heating and volumetric heating) that influences the dissolved gas expelling rates. Because the surface heating is different in the two cases given the drastically different NP densities on the surface (see Figure 1b,e), we studied a third case where we immersed the substrate with predeposited NPs in the NP suspension (case III) to better quantify the role of volumetric heating. With the same laser power of 1.1 W, we observed a much faster phase II bubble growth rate in case III than in case II (Figure 3a). By taking the difference of the phase II bubble growth rates (κ) of these two cases, the volume growth rate that can be attributed to volumetric heating in the suspension is $\sim 4 \times 10^4 \mu\text{m}^3/\text{s}$ (the volume growth rates difference in the two cases). This is more than 2 times larger than the growth rate by solely surface heating. For a phase II bubble, the mass influx of dissolved gas into the bubble (dm_g) is proportional to the change in local oversaturation ($d\zeta$) by the following formula:²⁷

$$dm_g = C_s V_w d\zeta \quad (1)$$

where C_s is the local air solubility in water and V_w is the volume of water contributing to the gas expelling for bubble growth, which depends on the thermal boundary layer thickness⁵⁰ at the bubble surface. $d\zeta$ is further proportional to the change in the local temperature surrounding the bubble (dT) by

$$d\zeta = -\frac{C_\infty}{C_s^2} \frac{dC_s}{dT} dT \quad (2)$$

where C_∞ is the gas saturation far away from the bubble. Combining eqs 1 and 2 (note $\frac{dC_s}{dT}$ is negative), it is clear that the increase in the temperature of liquid water surrounding the surface bubble (boundary layer)⁵⁰ will result in a positive local oversaturation, which further leads to the mass influx of dissolved air in the boundary layer expelling into surface bubble. This is the main cause of the phase II bubble growth.

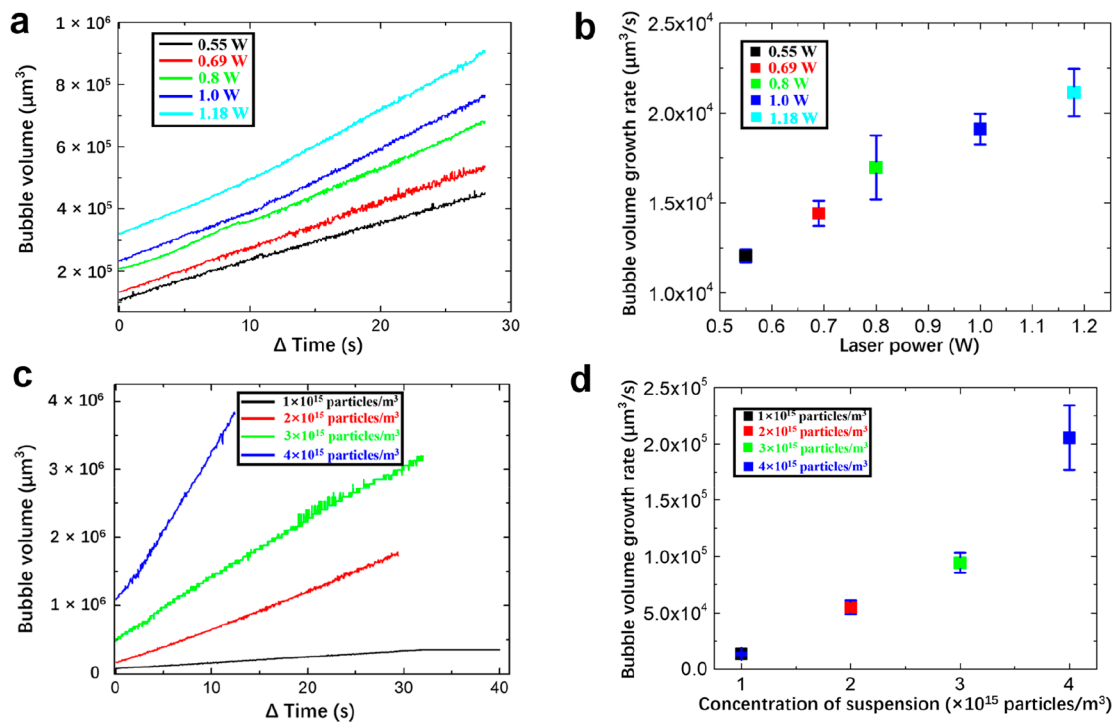


Figure 4. (a) Phase II surface bubble volume growth as a function of time under different laser powers from 0.55 to 1.18 W. The dissolved air concentration is 100%, and the Au NP concentration is 1×10^{15} particles/ m^3 for all cases. (b) Averaged phase II surface bubble volume growth rates under different laser powers. (c) Phase II surface bubble volume growth as a function of time in the NP suspensions with different concentrations of Au NPs. The dissolved air concentration of 100% and laser power of ~ 1.1 W are held constant for all cases. (d) Averaged phase II surface bubble volume growth rates in the NP suspensions with different concentrations of Au NPs.

To quantify the volumetric heating effect on the temperature around the bubble, we employ finite element simulations to investigate the temperature distribution under the two different heating geometries (see simulation details in the [Supporting Information](#), SI3). The simulated temperature profiles of the two heating conditions are shown in [Figure 3b,c](#). We can easily observe the difference in the locations and distributions of the hottest regions in the two cases as they are around the respective heating sources. The temperatures around the bubble surfaces are also different. [Figure 3d](#) shows the temperature at the bubble surfaces as a function of the arc length from the top to the bottom of the bubble. The overall bubble surface temperature in the volumetric heating case is higher than the one in the surface heating case, with the average temperature of the former 20 K higher than the latter. The reasons of this surface temperature difference are as follows: (1) In the surface heating case, there is significant heat loss from the heating source to the quartz substrate. (2) Most of the surface heater is in contact with the gas in the bubble, so the heat cannot be conducted to the bubble surface efficiently. (3) In the volumetric heating case, the thermocapillary flow of liquid near the surface of the bubble helps distribute heat around the bubble surface (see the velocity profile in [Figure 3e,f](#)). These simulation results indicate that volumetric heating is much more efficient in heating the surroundings of the bubble to a higher surface temperature, and this should be the main cause of the dramatically increased bubble growth rate.

The volumetric heating in the NP suspension provides additional means to control surface bubble growth via tuning the NP concentration in suspension, besides the conventional laser power control in surface heating methods. To study the effects of changing laser power, we tune the source laser power

from 0.3 to 1.12 W, which starts from the minimum laser power that can enable bubble nucleation to the maximum power achievable in our laser system. As plotted in [Figure 4a,b](#), the volume growth rate has only been increased by less than 2 times in this laser power range which changed 4 times. To examine the effects of changing Au NP concentration, we prepare the Au NP suspensions with four different NP concentrations from $\sim 1 \times 10^{15}$ to 4×10^{15} particles/ m^3 (see experimental details in the [Experimental Methods](#) section). Other experimental conditions, like laser power (~ 1.1 W) and dissolved air concentration (100%), are kept the same in all experiments. The phase II bubble volume growth as a function of time for the four different NP concentrations are all linear, but with significantly different slopes, and the growth rates are shown in [Figure 4d](#). As can be seen, the bubble volume growth rate is highly sensitive to the change of Au NP concentration, increasing by 1 order of magnitude with a 4-fold increase in NP concentration. On the basis of our comparisons, it is clear that NP suspension can provide a much more significant controllability on surface bubble growth compared to the effect from tuning the laser power. This will be beneficial for many microfluidics applications which desire widely tunable bubble sizes.¹⁶

CONCLUSION

To summarize, the growth dynamics of plasmonic surface bubbles in two cases, NP suspension (case I) and DI water with predeposited NPs on surface (case II), have been systematically investigated in this work. Because of the special volumetric heating geometry, NP suspension enables much higher bubble volume growth rates compared to the more conventional surface heating conditions. This is mainly

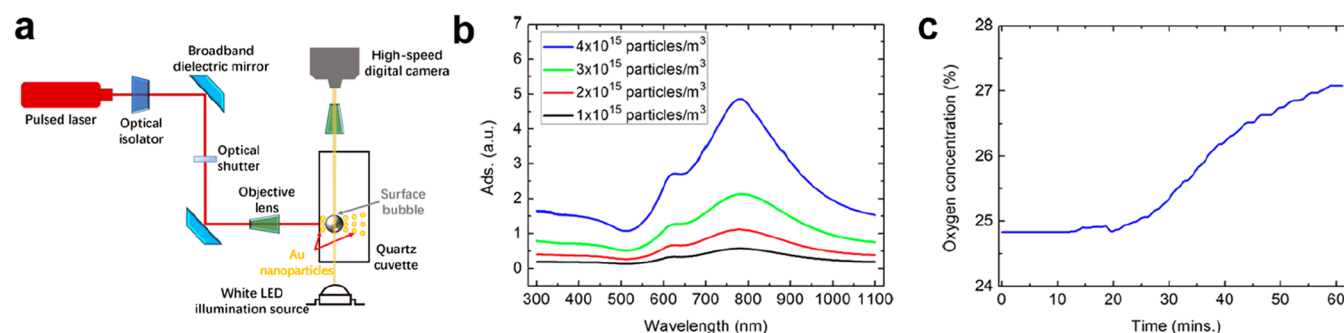


Figure 5. (a) Schematic of the experimental setup to characterize the growth dynamics of surface bubbles. (b) Measured absorption spectra for determining the Au NP concentrations in each suspension. The adsorption spectra of the suspensions with 1 to 4×10^{15} particles/ m^3 Au NP concentrations are plotted. (c) Oxygen concentration as a function of time of a degassed suspension as measured by using a Vernier Optical Dissolved Oxygen Probe. The degassing level can be kept in normal pressure for more than an hour with less than 5% increase.

because the volumetric heating geometry has a higher heating efficiency and can maintain a higher bubble surface temperature under the same laser power. We have also demonstrated that NP suspension can provide greater bubble growth tunability via changing the NP concentration. These results may provide fundamental insights into surface bubble growth dynamics in plasmonic suspensions. They may also offer additional degrees of freedom to control surface bubbles for microfluidics applications.

EXPERIMENTAL METHODS

Pulsed Laser. The mode-locked monochromatic femtosecond pulsed laser we used in our experiments is emitted from a Ti:sapphire crystal in an optical cavity (Spectra-Physics, Tsunami). The laser has a center wavelength of 800.32 nm and a full width at half-maximum length of ~ 10.5 nm. The laser power is in the range 0.3–1.2 W with the pulse duration of ~ 200 fs and the repetition rate of 80.7 MHz. The laser beam is guided by a series of broadband dielectric mirrors and finally focused by a 10 \times (Edmund Optics) objective lens to achieve a Gaussian intensity profile with a $1/e^2$ radius of 20 μm on the quartz surface. An optical shutter controlled by a digital controller (KDC101, Thorlabs) is used to turn on/off the laser (see Figure 5a).

High-Speed Videography. The plasmonic surface bubble growth dynamics is recorded by using a digital camera (HX-7, NAC). The digital camera is aligned to record the surface bubbles from the side view. A white LED illumination source and a 20 \times objective lens (Edmund Optics) are used in the video recording process (see Figure 5a). The videos recorded by the digital camera are then analyzed in a home-built MATLAB code, where the size of the surface bubble at each time frame is fitted. With these fitted results, we can then plot bubble volume as a function of time. The averaged phase II surface bubble volume growth rates and the error bars in Figures 2c and 4b,d are calculated based on the bubble volume growth rates measured in different trials under the same experimental condition. The frame rates for bubble video recording and bubble volume growth function plotting are 500 and 25 fps, respectively.

Au NP Suspension Preparation. The plasmonic Au NP suspension is prepared by ultrasonic dispersion of spherical Au NPs (Nanospectra Bioscience, Inc.) consisting of a silica core (~ 50 nm of radius) and an Au shell (~ 10 nm of thickness) in DI water. The resonant wavelength of the Au NPs in suspension is around 780–800 nm (average peak 785 nm) (see Figure 5b), and the concentration varies from case to case. In our experiment, the plasmonic NP suspension is contained in a quartz cuvette (Hellma, Sigma-Aldrich, 10 mm \times 10 mm). Before filled with suspension, the quartz cuvette is cleaned in an ultrasonic bath and dried at 150 $^\circ\text{C}$ for 10 min.

NP Predeposition. To predeposit a significant amount of Au NPs on the quartz surface, we first used pulsed laser to generate a large surface bubble (radius ~ 200 μm) on the surface in contact with the plasmonic NP suspension. Then, we generate another smaller surface

bubble (radius ~ 30 μm) very close to the large bubble. The growth of the smaller bubble is restricted by the nearby large one, as it will be swallowed by the larger bubble when they contact each other (see Movie S1). After that, a small amount of NPs can be deposited on the surface, and another smaller bubble will be generated at the same site shortly. By repeating this process tens of or even over a hundred times, we can eventually deposit a large amount of NPs on the quartz surface (see Figure 1e). Once we have accumulated significant amount of deposited NPs, we replaced the plasmonic NP suspension in the cuvette with DI water to prepare the experiment for case II. We note the specific technique to deposit the large amount of the NPs does influence the validity of the conclusion in the paper.

Water Degassing. The Au NP suspension is degassed in a sealed chamber pumped by an external mechanical pump. This is a physical way, which can pump out the dissolved oxygen and nitrogen simultaneously, given that the mass diffusivities of oxygen ($\sim 2.1 \times 10^{-5}$ cm^2/s) and nitrogen ($\sim 1.9 \times 10^{-5}$ cm^2/s) are close in water. The concentration of oxygen in the suspension can be feasibly measured by an oxygen sensor. Then, we can use the ratio of dissolved oxygen to quantize the concentration of dissolved air in the suspension.^{27,28} The concentration of oxygen is ~ 8.3 mg/L in the suspension without degassing. After 3 h degassing, the concentration of oxygen becomes $\sim 60\%$ of the original concentration; after 24 h degassing, the concentration of oxygen drops to $\sim 25\%$. These three degassing levels are found to be stable and highly repeatable. During experiments, the quartz cuvette containing degassed suspension is kept sealed to slow down the air redissolving process. Based on our tests, the concentration of oxygen increases less than 5% within 1.5 h while kept sealed in air (see Figure 5c). Because each of our experimental measurement normally lasts for less than 15 min, the concentration of oxygen in degassed suspension is considered to be constant.

ASSOCIATED CONTENT

Supporting Information

The Supporting Information is available free of charge at <https://pubs.acs.org/doi/10.1021/acsami.0c05448>.

SI1: characterizing the deposited Au NPs on quartz surface; SI2: surface bubble shrinkage study; SI3: finite element simulations details (PDF)

Movie S1 (MP4)

AUTHOR INFORMATION

Corresponding Authors

Tengfei Luo – Department of Aerospace and Mechanical Engineering, Department of Chemical and Biomolecular Engineering, and Center for Sustainable Energy of Notre Dame (ND Energy), University of Notre Dame, Notre Dame, Indiana

46556, United States; orcid.org/0000-0003-3940-8786;
Email: tluo@nd.edu

Eungkyu Lee – Department of Aerospace and Mechanical
Engineering, University of Notre Dame, Notre Dame, Indiana
46556, United States; orcid.org/0000-0002-0211-0727;
Email: elee18@nd.edu

Authors

Qiushi Zhang – Department of Aerospace and Mechanical
Engineering, University of Notre Dame, Notre Dame, Indiana
46556, United States; orcid.org/0000-0003-1313-7965

Robert Douglas Neal – College of Engineering, University of
Notre Dame, Notre Dame, Indiana 46556, United States

Dezhao Huang – Department of Aerospace and Mechanical
Engineering, University of Notre Dame, Notre Dame, Indiana
46556, United States; orcid.org/0000-0002-1413-5438

Svetlana Neretina – College of Engineering and Department of
Chemical and Biomolecular Engineering, University of Notre
Dame, Notre Dame, Indiana 46556, United States;
orcid.org/0000-0002-6889-4384

Complete contact information is available at:
<https://pubs.acs.org/10.1021/acsami.0c05448>

Notes

The authors declare no competing financial interest.

ACKNOWLEDGMENTS

This work is supported by National Science Foundation (1706039 and 1937923) and the Center for the Advancement of Science in Space (GA-2018-268). T.L. thanks the support from the Dorini Family endowed professorship in energy studies. S.N. acknowledges the support of a National Science Foundation Award (DMR-1803917).

REFERENCES

- (1) Neumann, O.; Urban, A. S.; Day, J.; Lal, S.; Nordlander, P.; Halas, N. J. Solar Vapor Generation Enabled by Nanoparticles. *ACS Nano* **2013**, *7* (1), 42–49.
- (2) Baffou, G.; Quidant, R. Nanoplasmonics for Chemistry. *Chem. Soc. Rev.* **2014**, *43*, 3898–3907.
- (3) Carlson, M. T.; Green, A. J.; Richardson, H. H. Superheating Water by CW Excitation of Gold Nanodots. *Nano Lett.* **2012**, *12* (3), 1534–1537.
- (4) Fang, Z.; Zhen, Y.; Neumann, O.; Polman, A.; de Abajo, de F. J. G.; Ordlander, P.; Halas, N. J. Evolution of Light-Induced Vapor Generation at a Liquid-Immersed Metallic Nanoparticle. *Nano Lett.* **2013**, *13* (4), 1736–1742.
- (5) Baral, S.; Green, A. J.; Livshits, M. Y.; Govorov, A. O.; Richardson, H. H. Comparison of Vapor Formation of Water at the Solid/Water Interface to Colloidal Solutions Using Optically Excited Gold Nanostructures. *ACS Nano* **2014**, *8* (2), 1439–1448.
- (6) Liu, X.; Bao, L.; Dipalo, M.; De Angelis, F.; Zhang, X. Formation and Dissolution of Microbubbles on Highly-Ordered Plasmonic Nanopillar Arrays. *Sci. Rep.* **2016**, *5*, 18515.
- (7) Emelianov, S. Y.; Li, P.; O'Donnell, M. Photoacoustics for Molecular Imaging and Therapy. *Phys. Today* **2009**, *62* (8), 34–39.
- (8) Kim, C.; Cho, E. C.; Chen, J.; Song, K. H.; Au, L.; Favazza, C.; Zhang, Q.; Cogley, C. M.; Gao, F.; Xia, Y.; Wang, L. V. In Vivo Molecular Photoacoustic Tomography of Melanomas Targeted by Bioconjugated Gold Nanocages. *ACS Nano* **2010**, *4* (8), 4559–4564.
- (9) Maier, C. M.; Huergo, M. A.; Milosevic, S.; Pernpeintner, C.; Li, M.; Singh, D. P.; Walker, D.; Fischer, P.; Feldmann, J.; Lohmuller, T. Optical and Thermophoretic Control of Janus Nanoparticle Injection into Living Cells. *Nano Lett.* **2018**, *18* (12), 7935–7941.
- (10) Zhang, T.; Li, S.; Du, Y.; He, T.; Shen, Y.; Bai, C.; Huang, Y.; Zhou, X. Revealing the Activity Distribution of a Single Nanocatalyst by Locating Single Nanobubbles with Super-Resolution Microscopy. *J. Phys. Chem. Lett.* **2018**, *9* (18), 5630–5635.
- (11) Lapotko, D. Plasmonic Nanoparticle-Generated Photothermal Bubbles and Their Biomedical Applications. *Nanomedicine* **2009**, *4* (7), 813–845.
- (12) Metwally, K.; Mensah, S.; Baffou, G. Fluence Threshold for Photothermal Bubble Generation Using Plasmonic Nanoparticles. *J. Phys. Chem. C* **2015**, *119* (51), 28586–28596.
- (13) Lachaine, R.; Boutopoulos, C.; Lajoie, P.-Y.; Boulais, É.; Meunier, M. Rational Design of Plasmonic Nanoparticles for Enhanced Cavitation and Cell Perforation. *Nano Lett.* **2016**, *16* (5), 3187–3194.
- (14) Shao, J.; Xuan, M.; Dai, L.; Si, T.; Li, J.; He, Q. Near-Infrared-Activated Nanocalorifiers in Microcapsules: Vapor Bubble Generation for In Vivo Enhanced Cancer Therapy. *Angew. Chem., Int. Ed.* **2015**, *54* (43), 12782–12787.
- (15) Liu, H. L.; Fan, C. H.; Ting, C. Y.; Yeh, C. K. Combining Microbubbles and Ultrasound for Drug Delivery to Brain Tumors: Current Progress and Overview. *Theranostics* **2014**, *4* (4), 432–444.
- (16) Prakash, M.; Gershenfeld, N. Microfluidic Bubble Logic. *Science* **2007**, *315* (5813), 832–835.
- (17) Barcikowski, S.; Devesa, F.; Moldenhauer, K. Impact and Structure of Literature on Nanoparticle Generation by Laser Ablation in Liquids. *J. Nanopart. Res.* **2009**, *11*, 1883–1893.
- (18) Barcikowski, S.; Compagnini, G. Advanced Nanoparticle Generation and Excitation by Lasers in Liquids. *Phys. Chem. Chem. Phys.* **2013**, *15*, 3022–3026.
- (19) Huang, H.; Lai, J.; Lu, J.; Li, Z. Pulsed Laser Ablation of Bulk Target and Particle Products in Liquid for Nanomaterial Fabrication. *AIP Adv.* **2019**, *9*, 015307.
- (20) Yan, Z.; Chrisey, D. B. Pulsed Laser Ablation in Liquid for Micro-/Nanostructure Generation. *J. Photochem. Photobiol., C* **2012**, *13* (3), 204–223.
- (21) Wagener, P.; Ibrahimkutty, S.; Menzel, A.; Plech, A.; Barcikowski, S. Dynamics of Silver Nanoparticle Formation and Agglomeration inside the Cavitation Bubble after Pulsed Laser Ablation in Liquid. *Phys. Chem. Chem. Phys.* **2013**, *15*, 3068–3074.
- (22) Reich, S.; Schönfeld, P.; Wagener, P.; Letzel, A.; Ibrahimkutty, S.; Gökce, B.; Barcikowski, S.; Menzel, A.; Dos Santos Rolo, T.; Plech, A. Pulsed Laser Ablation in Liquids: Impact of the Bubble Dynamics on Particle Formation. *J. Colloid Interface Sci.* **2017**, *489*, 106–113.
- (23) Lam, J.; Lombard, J.; Dujardin, C.; Ledoux, G.; Merabia, S.; Amans, D. Dynamical Study of Bubble Expansion Following Laser Ablation in Liquids. *Appl. Phys. Lett.* **2016**, *108*, 074104.
- (24) Xie, Y.; Zhao, C. An Optothermally Generated Surface Bubble and Its Applications. *Nanoscale* **2017**, *9*, 6622–6631.
- (25) Karim, F.; Vasquez, E. S.; Sun, Y.; Zhao, C. Optothermal Microbubble Assisted Manufacturing of Nanoparticle-Rich Structures for Active Chemical Sensing. *Nanoscale* **2019**, *11*, 20589–20597.
- (26) Karim, F.; Vasquez, E. S.; Zhao, C. Fabricated Nanoparticle-Rich Plasmonic Nanostructures Through an Optothermal Surface Bubble in a Droplet. *Opt. Lett.* **2018**, *43* (2), 334–336.
- (27) Wang, Y.; Zaytsev, M. E.; The, H. L.; Eijkel, J. C. T.; Zandvliet, H. J. W.; Zhang, X.; Lohse, D. Vapor and Gas-Bubble Growth Dynamics around Laser-Irradiated, Water-Immersed Plasmonic Nanoparticles. *ACS Nano* **2017**, *11* (2), 2045–2051.
- (28) Wang, Y.; Zaytsev, M. E.; Lajoie, G.; The, H. L.; Eijkel, J. C. T.; van den Berg, A.; Versluis, M.; Weckhuysen, B. M.; Zhang, X.; Zandvliet, H. J. W.; Lohse, D. Giant and Explosive Plasmonic Bubbles by Delayed Nucleation. *Proc. Natl. Acad. Sci. U. S. A.* **2018**, *115* (30), 7676–7681.
- (29) Baffou, G.; Polleux, J.; Rigneault, H.; Monneret, S. Superheating and Micro-Bubble Generation around Plasmonic Nanoparticles under cw Illumination. *J. Phys. Chem. C* **2014**, *118* (9), 4890–4898.
- (30) Zaytsev, M. E.; Wang, Y.; Zhang, Y.; Lajoie, G.; Zhang, X.; Prosperetti, A.; Zandvliet, H. J. W.; Lohse, D. Gas–Vapor Interplay in

Plasmonic Bubble Shrinkage. *J. Phys. Chem. C* **2020**, *124* (10), 5861–5869.

(31) Chen, J.; Saklayen, N.; Courvoisier, S.; Shen, Z.; Lu, J.; Ni, X.; Mazur, E. Dynamics of Transient Microbubbles Generated by fs-Laser Irradiation of Plasmonic Micropyramids. *Appl. Phys. Lett.* **2017**, *110*, 153102.

(32) Miniewicz, A.; Bartkiewicz, S.; Orlikowska, H.; Dradrach, K. Marangoni Effect Visualized in Two-Dimensions Optical Tweezers for Gas Bubbles. *Sci. Rep.* **2016**, *6*, 34787.

(33) Zou, A.; Gupta, M.; Maroo, S. C. Origin, Evolution, and Movement of Microlayer in Pool Boiling. *J. Phys. Chem. Lett.* **2018**, *9* (14), 3863–3869.

(34) Zhao, C.; Xie, Y.; Mao, Z.; Zhao, Y.; Rufo, J.; Yang, S.; Guo, F.; Mai, J. D.; Huang, T. J. Theory and Experiment on Particle Trapping and Manipulation via Optothermally Generated Bubbles. *Lab Chip* **2014**, *14* (2), 384–391.

(35) Lin, L.; Peng, X.; Mao, Z.; Li, W.; Yogeesh, M. N.; Rajeeva, B. B.; Perillo, E. P.; Dunn, A. K.; Akinwande, D.; Zheng, Y. Bubble-Pen Lithography. *Nano Lett.* **2016**, *16* (1), 701–708.

(36) Namura, K.; Nakajima, K.; Suzuki, M. Quasi-Stokeslet Induced by Thermoplasmonic Marangoni Effect around a Water Vapor Microbubble. *Sci. Rep.* **2017**, *7*, 45776.

(37) Namura, K.; Shimada, Y.; Okai, S.; Kumar, S.; Suzuki, M. Thermoplasmonics for Investigation of Microbubble Dynamics in Degassed Water. *Proc. SPIE 11082, Plasmonics: Design, Materials, Fabrication, Characterization, and Applications XVII* **2019**, 110820S; 27.

(38) Namura, K.; Nakajima, K.; Kimura, K.; Suzuki, M. Photo-thermally Controlled Marangoni Flow around a Micro Bubble. *Appl. Phys. Lett.* **2015**, *106*, 043101.

(39) Namura, K.; Nakajima, K.; Suzuki, M. Investigation of Transition from Thermal- to Solutal-Marangoni Flow in Dilute Alcohol/Water Mixtures Using Nano-Plasmonic Heaters. *Nanotechnology* **2018**, *29* (6), 065201.

(40) Richardson, H. H.; Carlson, M. T.; Tandler, P. J.; Hernandez, P.; Govorov, A. O. Experimental and Theoretical Studies of Light-to-Heat Conversion and Collective Heating Effects in Metal Nanoparticle Solutions. *Nano Lett.* **2009**, *9* (3), 1139–1146.

(41) Armon, N.; Greenberg, E.; Layani, M.; Rosen, Y. S.; Magdassi, S.; Shpaysman, H. Continuous Nanoparticle Assembly by a Modulated Photo-Induced Microbubble for Fabrication of Micro-metric Conductive Patterns. *ACS Appl. Mater. Interfaces* **2017**, *9* (50), 44214–44221.

(42) Zhang, Q.; Pang, Y.; Schiffbauer, J.; Jemcov, A.; Chang, H.; Lee, E.; Luo, T. Light-Guided Surface Plasmonic Bubble Movement via Contact Line De-Pinning by In-Situ Deposited Plasmonic Nanoparticle Heating. *ACS Appl. Mater. Interfaces* **2019**, *11* (51), 48525–48532.

(43) Moon, S.; Zhang, Q.; Huang, D.; Senapati, S.; Chang, H.-C.; Lee, E.; Luo, T. Biocompatible Direct Deposition of Functionalized Nanoparticles using Shrinking Surface Plasmonic Bubble. ChemRxiv, DOI: 10.26434/chemrxiv.11901513.

(44) Lee, E.; Huang, D.; Luo, T. Ballistic Supercavitating Nano Swimmer Driven by Single Gaussian Beam Optical Pushing and Pulling Forces; ArXiv.

(45) Nikolayev, V. S.; Beysens, D. A. Boiling Crisis and Non-Equilibrium Drying Transition. *Europhys. Lett.* **1999**, *47* (3), 345–351.

(46) Frost, W.; Kippenhan, C. J. Bubble Growth and Heat-Transfer Mechanisms in the Forced Convection Boiling of Water Containing a Surface Active Agent. *Int. J. Heat Mass Transfer* **1967**, *10* (7), 931–936.

(47) Malkus, J. S.; Scorer, R. S.; Ludlam, F. H.; Bjorgum, O. Bubble Theory of Penetrative Convection. *Q. J. R. Meteorol. Soc.* **1953**, *79* (340), 288–293.

(48) Yang, X.; Karnbach, F.; Uhlemann, M.; Odenbach, S.; Eckert, K. Dynamics of Single Hydrogen Bubbles at a Platinum Micro-electrode. *Langmuir* **2015**, *31* (29), 8184–8193.

(49) Hao, Y.; Zhang, Y.; Prosperetti, A. Mechanics of Gas-Vapor Bubbles. *Phys. Rev. Fluids* **2017**, *2*, 034303.

(50) Enriquez, O.; Sun, C.; Lohse, D.; Prosperetti, A.; Van Der Meer, D. The Quasi-Static Growth of CO₂ Bubbles. *J. Fluid Mech.* **2014**, *741*, R1.